

See discussions, stats, and author profiles for this publication at: <https://www.researchgate.net/publication/257202830>

Pt@CeO₂ Multicore@Shell Self-Assembled Nanospheres: Clean Synthesis, Structure Optimization, and Catalytic Applications

ARTICLE in JOURNAL OF THE AMERICAN CHEMICAL SOCIETY · SEPTEMBER 2013

Impact Factor: 12.11 · DOI: 10.1021/ja4069134 · Source: PubMed

CITATIONS

70

READS

102

4 AUTHORS, INCLUDING:



Xiao Wang

Tianjin University

258 PUBLICATIONS 2,104 CITATIONS

SEE PROFILE



Da-Peng Liu

Chinese Academy of Sciences

42 PUBLICATIONS 1,083 CITATIONS

SEE PROFILE



Hongjie Zhang

Chinese Academy of Sciences

428 PUBLICATIONS 11,874 CITATIONS

SEE PROFILE

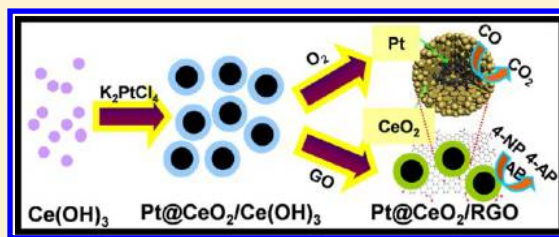
Pt@CeO₂ Multicore@Shell Self-Assembled Nanospheres: Clean Synthesis, Structure Optimization, and Catalytic Applications

Xiao Wang, Dapeng Liu, Shuyan Song, and Hongjie Zhang*

State Key Laboratory of Rare Earth Resource Utilization, Changchun Institute of Applied Chemistry, Chinese Academy of Sciences, Changchun, 130022 Jilin, China

Supporting Information

ABSTRACT: A clean nonorganic synthetic method has been developed to fabricate the uniform pomegranate-like Pt@CeO₂ multicore@shell nanospheres in a large scale. Under the effective protection of Ar atmosphere the redox reaction just simply happened between Ce(NO₃)₃ and K₂PtCl₄ in an alkaline aqueous solution, in which no other reducing agents or surfactants were added. The as-obtained nanospheres exhibited excellent structure stability even being calcined at 600 °C for 5 h. Moreover, the as-obtained Pt@CeO₂ multicore@shell nanospheres can be further supported on reduced graphene oxide (RGO) to form heterogeneous nanocatalyst, which has been successfully applied in the chemical reduction reaction of nitrophenol (NP) by ammonia borane (NH₃BH₃, dubbed as AB) instead of hazardous H₂ or NaBH₄.



1. INTRODUCTION

As one of the most important catalysts, Pt-CeO₂ systems have drawn continuous attention because of their highly enhanced catalytic performance and wide range of applications.^{1–9} To meet practical needs, Pt-based catalysts are often required to work at relatively high temperatures. However, under such conditions, nanoparticle catalysts are apt to aggregate to minimize their surface energy, resulting in the heavy loss of catalytic active centers and serious catalytic degradation and even inactivation. Therefore, the synthesis of high-temperature-stable Pt-CeO₂ catalysts has become an area of great focus in material science. For a thermally stable catalyst, three requirements must be simultaneously satisfied:¹⁰ (1) their components should be chemically inert while working in specified atmospheres (air is the most common one); (2) there should be no mass transformation during high-temperature treatment; and (3) after calcination, the active centers should maintain their catalytic activities.

However, simply loading Pt on metal oxides cannot achieve the above goals. Therefore, the fabrication of complex hybrids with well-designed and controlled secondary nanostructures has been explored and has been shown to be one of the most efficient ways to achieve these goals. In the case of noble metals, especially Au, two main structure modulations can significantly improve their high-temperature stability. One is embedding small-sized noble metal nanoparticles into highly stable porous inorganic nanostructures (CeO₂, TiO₂, SiO₂, ZrO₂, etc.).^{11,12} The other is encapsulating noble metal nanoparticles within metal oxides to form core@shell^{13–18} or yolk@shell^{19–22} nanostructures. The inert metal oxides in both of the two types of hybrids play the key role of physically separating the noble metal nanoparticles from each other. This effective steric hindrance by the metal oxides favors these noble

metal nanoparticles keeping their original shape, size, surface state, and catalytic activity.

There are only a few reports on the preparation of high-temperature-stable Pt-CeO₂ catalysts. A representative work has been done by Yan's group,² where they synthesized thermally stable Pt-CeO₂ hybrids by protection with SiO₂. The oil-phase prepared CeO₂ nanoparticles had good uniformity, and the thin SiO₂ layer was effective at maintaining the size and shape of the Pt particles under high-temperature treatment. After etching away the SiO₂ shell, the residual Pt-CeO₂ particles still exhibited high catalytic performance during the catalytic conversion of CO into CO₂.

It is hard to synthesize classic high-temperature-stable nanocatalysts without the aid of surface silanization to form inert silica layers, whose surfaces are rich in hydroxyl groups that can facilitate further linkage of a second component. However, such layer-by-layer technology is a multistep process that requires precise control and complex surface modification, so it is not conducive to large-scale synthesis and has seriously limited the applications of such catalysts. Most recently, synthesis strategies wherein a metal salt is reduced in situ with the support material without the addition of any other surfactants, also known as clean synthesis strategies, have received a great deal of attention for preparing noble metal-based hybrid catalysts.^{23–27} Because of the clean particle surfaces and the strong binding force between the different components of hybrids, the as-obtained nanocatalysts have shown excellent catalytic performance. For instance, through an in situ redox reaction between the reductive WO_{2.72} substrate and the oxidative noble-metal salt precursors,²³ a series of noble

Received: July 10, 2013

Published: September 29, 2013



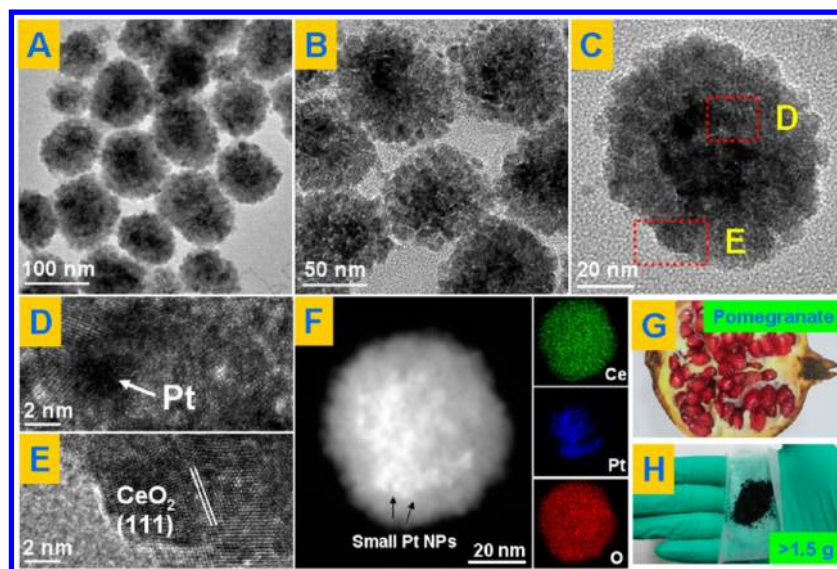


Figure 1. (A–E) TEM and (F) STEM images of the pomegranate-like Pt@CeO₂ multicore@shell nanospheres; (G) profile of a real pomegranate; (H) products prepared in one pot.

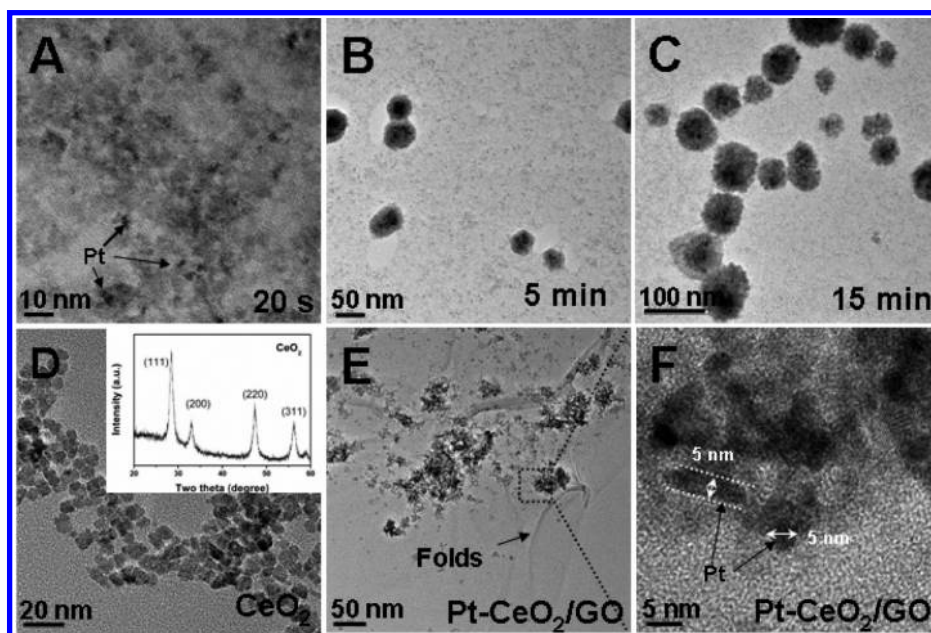


Figure 2. TEM images of the Pt@CeO₂ nanospheres: after reaction for 20 s (A), 5 min (B), and 15 min (C); without addition of K₂PtCl₄ (D); introduction of GO (E and F).

metal/WO₃ nanocomposites with uniform metal dispersion, tunable metal particle size, and narrow metal particle size distribution were obtained without addition of any reducing agent or surfactants. A clean synthesis route has also been developed in a Ag-CeO₂ system^{26,27} by fabricating an autocatalyzed reaction between Ce(OH)₃ and Ag(NH₃)₂⁺ to form rice-ball like hybrid nanostructures with high catalytic activity. However, there is still no such report for the very important Pt-CeO₂ catalyst system. Thus, it seems meaningful to develop an effective way to realize the facile, clean, and one-pot synthesis of highly active and high-temperature-stable Pt-CeO₂ hybrids in a large scale.

In our previous works,^{28–30} we observed that when Ce³⁺ aqueous solutions were made alkaline, the color of the solution turns slightly yellow and then brown, which indicates the typical oxidation process of Ce³⁺ into Ce⁴⁺ by O₂ in air. These

results indicate that the reducing capability of Ce³⁺ is stronger under alkaline conditions than under neutral ones. Therefore, choosing a Pt salt precursor with the proper oxidation potential will allow the redox between Ce³⁺ and Pt precursor to occur and could also lead to the spontaneous formation of a hybrid structure. Deoxygenation during the reaction is important in order to ensure that the Ce³⁺ ions will be oxidized by the Pt precursor and not by O₂. In addition, NaOH is used instead of organic amines in order to avoid introduction of a second reducing agent in the system. The mutual inhibition effect between CeO₂ and Pt makes their hybrids rather stable and able to keep their size, shape, and structure.

2. RESULTS AND DISCUSSION

2.1. Pt@CeO₂ Multicore@Shell Nanospheres.

2.1.1. Characterizations. The transmission electron microscope (TEM) images in Figure 1 show that the as-obtained Pt@CeO₂ hybrids are uniform 84.8 nm (average particle size, the size-distributions are shown in Figure S2 of the Supporting Information) nanospheres with a pomegranate-like multicore@shell superstructure. In any hybrid nanosphere, the shell is built up by hundreds of CeO₂ nanoparticles with an average size of 6.2 nm. The Pt nanoparticles beneath the shell can be distinguished by their deeper contrast from CeO₂. The Pt nanoparticles are separately imbedded in the CeO₂ polymer network and tend to be located in the center of the superstructure. It can be seen from the HRTEM images in Figure 1D,E of the specific core and shell parts of Figure 1C that the lattice spacing (0.31 nm) corresponds well with the characteristic (111) planes of fluorite phase CeO₂. However, the dense CeO₂ coating makes it hard to observe any clear crystal planes of Pt. The individual 3–5 nm Pt cores could be distinguished in Figure 1F. The corresponding STEM image (Figure 1F) and the selective EDX spectra (Supporting Information, Figure S4) of the hybrid nanosphere firmly identify its pomegranate-like multicore@shell superstructure (Figure 1G), in which Ce and O elements spread everywhere and Pt only exists in the center of the nanosphere. The concentration of Pt in Pt@CeO₂ was tested by ICP, the value was about 8.7 wt %. Here, it should be noted that our clean and fast method can easily realize the large-scale synthesis of products, such that 1.5 g of the multicore@shell nanospheres have been produced in one pot (Figure 1H).

2.1.2. Structure Formation Mechanism. The mechanism for the formation of the multicore@shell spherical superstructures has been discussed in detail according to their time-evolution TEM images. The superstructure formation experienced two stages, that is, the nucleation–growth of Pt and CeO₂ nanoparticles and the self-assembly of the two components. In the nucleation–growth stage, the zeta potential testing indicates the positive surface (+25.9 mV) of Ce(OH)₃ obtained through the reaction of Ce³⁺ and NaOH. Then the following introduced PtCl₄²⁻ anions would be firmly attracted on Ce(OH)₃ surface via electrostatic interactions. In Figure 2A, the TEM image clearly identified this phenomenon. As a result, when the autoredox reaction happened between Ce(OH)₃ and K₂PtCl₄, ultrasmall Pt and CeO₂ nanoparticles were formed and every Pt particle has been firmly enclosed by several CeO₂ nanoparticles, forming the original Pt–CeO₂ self-assembled hybrid structures (as depicted in Figure 3). Elsewhere, CeO₂ nanoparticles were randomly distributed and no ordered self-assembly structure could be observed. The absence of surface modification on both Pt and CeO₂ means that the nanoparticles are naked on their surfaces and are thus unstable. The

nanoparticles need further growth or aggregation to decrease the whole system's energy driven by thermodynamic equilibrium in the following self-assembly stage, so after reaction from 5 (Figure 2B) to 15 min (Figure 2C), we can see that these original Pt–CeO₂ hybrids have self-assembled into larger and larger pomegranate-like multicore@shell superstructures with an overall spherical shape, finally achieving stability when the system reaches a size of about 85 nm.

Consider that the whole synthetic process was performed via redox reaction between Ce(NO₃)₃ and K₂PtCl₄ under alkaline conditions without any other components, so the hybrid superstructure formation should only be related to the growth balance between CeO₂ and Pt nanoparticles. Thus, two control experiments have been carried out to identify the balancing forces in this formation process. The first control experiment is performed under the same reaction conditions, except for addition of K₂PtCl₄ and protection of inert atmosphere. It can be seen in Figure 2D that no self-assembled 3D nanostructures were formed, and only monodisperse sub-8.0 nm CeO₂ nanoparticles were formed due to oxidation by O₂, whereas the CeO₂ nanoparticles in the hybrid reaction were 6.2 nm in size. The other control experiment was done by directly introducing graphene oxide (GO) into the reaction system to alter the growth of the nanoparticles. Because of its abundant functional groups, GO is a good substrate to restrict the growth and dispersion of nanoparticles and finally enable the formation of stable nanoparticles/reduced graphene oxide (RGO) hybrids.^{24,31–33} As expected, only Pt–CeO₂–GO ternary hybrid nanocomposites were produced, rather than any ordered core@shell spherical superstructures. The Pt and CeO₂ nanoparticles distributed on the RGO surface nonuniformly in very large size distributions (Figure 2E,F).

2.1.3. CO Catalytic Oxidation. Five samples with the same molar ratio of [Pt]/[Ce] were chosen to investigate the influence of the Pt–CeO₂ hybrid structures on their catalytic performance. Sample 1 is the as-obtained Pt@CeO₂ nanospheres; sample 2 was obtained by calcining sample 1 at 450 °C for 5 h in air; sample 3 was obtained by calcining sample 1 at 600 °C for 5 h in air; sample 4 was obtained by directly mixing prepared PVP-stabilized Pt and bare CeO₂ nanoparticles together; sample 5 was obtained by calcining sample 4 at 600 °C for 5 h in air. The TEM images of sample 2 (Figure 4A) and sample 3 (Figure 4B) show that there was no obvious growth or aggregation of the multicore@shell Pt@CeO₂ nanospheres in good consistence with the result of particle size analysis (Supporting Information, Figure S4). Their size, shape, and hybrid superstructure were well maintained. However, the simple mixture of Pt and CeO₂ nanoparticles (sample 5) was rather unstable, as the particles aggregated heavily and the Pt nanoparticles increased in size from 4 nm to over 20 nm after calcination (Supporting Information, Figure S8). These results indicate that the as-obtained pomegranate-like multicore@shell superstructures indeed work well at protecting the Pt nanoparticles, even under long-term high-temperature heat treatment.

Composites of Pt and CeO₂ are some of the most prevalent catalysts in the fields of exhaust emission control and fuel cells, so our samples were evaluated by their performance in catalyzing CO oxidization. As shown in Figure 4C, it was found that for the conversion of CO into CO₂, the 100% conversion temperature of the five samples follows such a sequence: sample 1 (140 °C) < sample 2 = sample 3 (145 °C) < sample 4 (170 °C) < sample 5 (300 °C). This means the

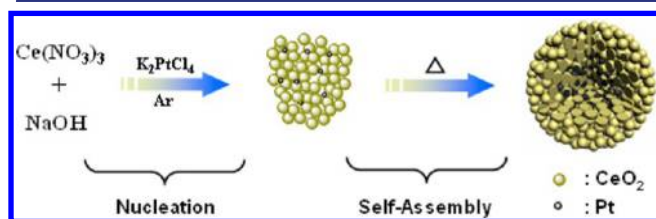


Figure 3. Schematic structure formation of the pomegranate-like Pt@CeO₂ multicore@shell nanospheres.

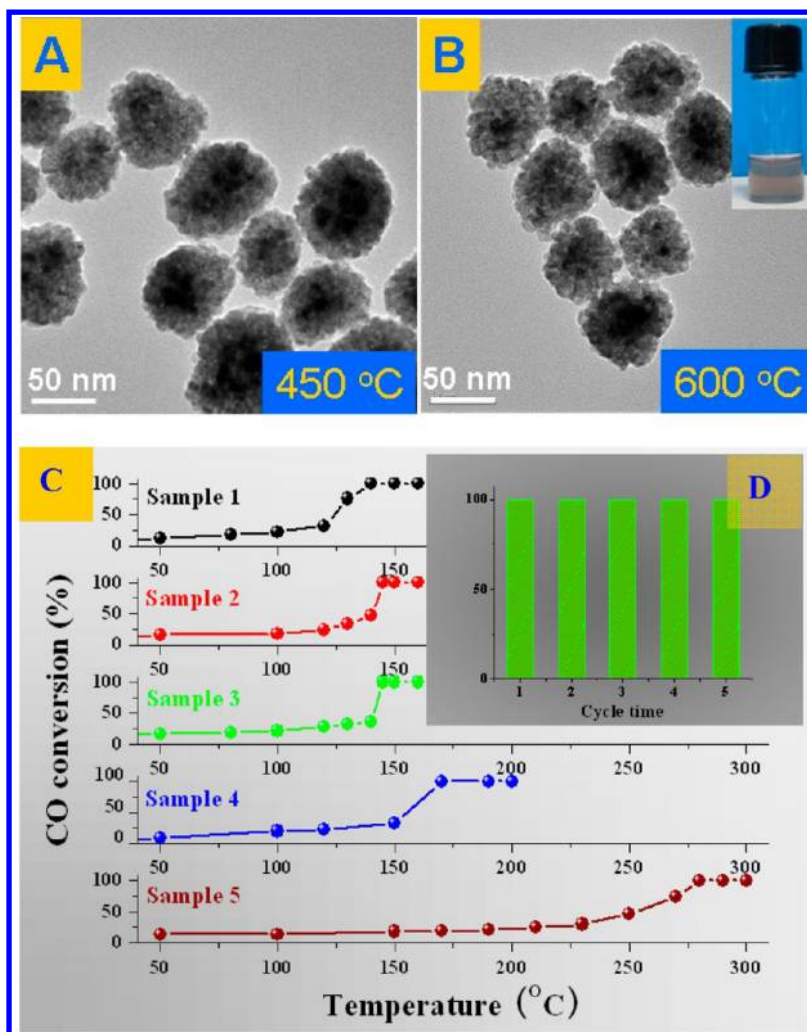


Figure 4. TEM images of (A) sample 2 and (B) sample 3 (the scale bar in A and B is 50 nm); (C) CO conversion curves of samples 1–5; (D) catalytic cycles of sample 3 at 150 °C. Every 8 mg of catalysts were mixed with 20 mg of SiO₂ (the SiO₂ powder was purchased from Aladdin company with particle size of 15 nm ± 5 nm).

samples with the core@shell structure (samples 1–3) exhibited much higher activity and stability than the physically blended samples (samples 4 and 5), which could be attributed to the synergistic effect between Pt and CeO₂. It was well-known that the synergistic effect only appeared when the two composites were close enough. There was no doubt that Pt and CeO₂ in Pt@CeO₂ were much closer than them in the physically blended samples because of the interface redox reaction. So the synergistic effect must be stronger in Pt@CeO₂. Compared to sample 1, the activities of sample 2 and 3 were slightly decreased. In the case of sample 4, calcination resulted in fast growth of Pt and aggregation of CeO₂ (Supporting Information, Figure S7C,D), and hence its activity degraded heavily. In addition, such core@shell hybrid nanospheres which obtained by our simple synthesis exhibited the similar catalytic activity of the classic Pt-CeO₂ catalyst which obtained via a complex multistep method.² Next, a cycling test was done to study the stability of sample 3 by repeated heat treatment in 1% CO gas (Figure 4 inside). After five successful cycles from 600 to 150 °C, sample 3 still maintained a 100% conversion rate of CO into CO₂. The result clearly shows that the as-obtained pomegranate-like Pt@CeO₂ multicore@shell catalyst is stable and active under long-term high-temperature catalytic conditions. Some related experimental data, such as GHSV, specific

surface areas, pore sizes, and TOFs, have been listed in Table S1 of the Supporting Information.

2.2. Pt@CeO₂ Multicore@Shell Nanospheres Supported on RGO (Pt@CeO₂/RGO). **2.2.1. Structure Optimization.** The Pt@CeO₂ multicore@shell nanospheres indeed exhibit high activity and stability in the heterogeneous catalytic reaction (CO oxidation) even after high-temperature calcination; however, they might not be suitable for a homogeneous catalytic reaction due to their extremely good colloidal stability in water (as shown in Supporting Information Figure S11A). Once the catalysts are dispersed in water, it is difficult to collect the expensive noble metal catalysts after the reaction such that they can not even be completely separated by centrifugation at 12 000 rpm. Fortunately, the development of graphene science has easily resolved this problem. When graphene is used as a substrate, it can gather the active centers together; however, the active components still retain their original shape, size, and surface state. In addition, the graphene-supporting catalysts show poorer colloidal stability compared to the original catalysts because of a decrease in Brownian motions; thus, they can be easily separated from the reaction system as a bulk material. This separation is very helpful for collecting and recycling expensive Pt catalysts after liquid catalytic reactions.

Thus graphene was chosen here as the second substrate to load the Pt@CeO₂ multicore@shell nanospheres.

2.2.2. Characterizations. Photos of the obtained Pt@CeO₂ nanospheres and Pt@CeO₂/RGO hybrid nanocomposites are shown in Supporting Information Figure S11. It can be clearly observed that Pt@CeO₂ is well dispersed in water but that Pt@CeO₂/RGO is gathered at the bottom of the flask. A self-separating effect is observed. The detailed synthetic process is described in Supporting Information Figure S12.

The X-ray diffraction (XRD) patterns of Pt@CeO₂/RGO and GO are shown in Supporting Information Figure S13. In contrast to the characteristic diffraction peak of disordered GO, the peak at $2\theta = 10.6^\circ$ disappeared in Pt@CeO₂/RGO, indicating the complete reduction of GO. The peaks at $2\theta = 28.5^\circ$, 33.0° , 47.4° , and 56.3° can be indexed into the (111), (200), (220), and (311) reflections (JCPDS No. 34-0394) of fluorite-phase CeO₂, respectively. Although no obvious diffraction peaks of Pt are observed in the XRD pattern of Pt@CeO₂/RGO, the presence of Pt was confirmed by STEM, XPS, and EDX analysis (as shown in Figures 5 and 6 and Supporting Information Figure S14, respectively).

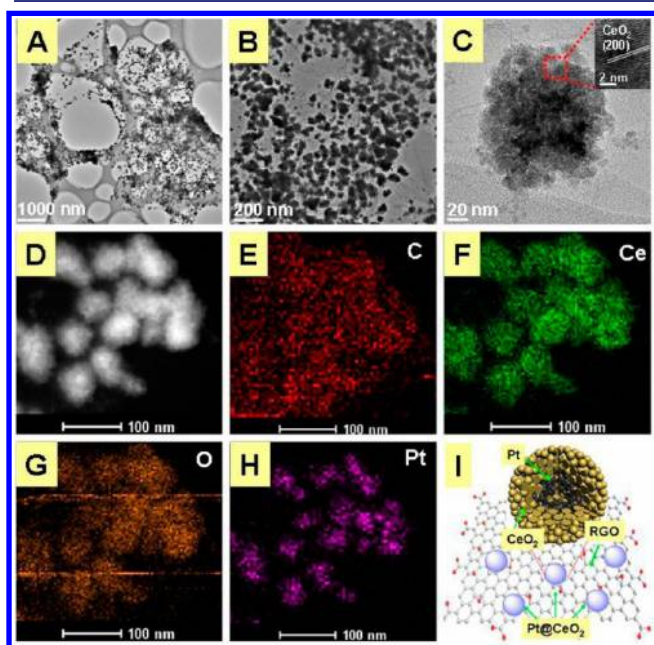


Figure 5. TEM images of the Pt@CeO₂/RGO hybrid nanocomposites (A–C), the corresponding STEM image (D) and EDX mapping analysis (E: carbon; F: cerium; G: oxygen; and H: platinum), and the structure diagram of Pt@CeO₂/RGO.

The transmission electron microscope (TEM) images in Figure 5 show that the as-obtained Pt@CeO₂ multicore@shell nanospheres were loaded onto the RGO surface uniformly. No scattered nanoparticles are found outside the RGO nanosheets. The lattice spacing of 0.27 nm corresponds well to the (200) characteristic planes of fluorite-phase CeO₂. The element distributions were analyzed using mapping analysis, shown in Figure 5D–H. It is clearly observed that each nanosphere encapsulates tens of discontinuous Pt nanoparticles inside.

To determine the oxidation state of carbon in Pt@CeO₂/RGO, XPS analysis was performed, and the results are shown in Figure 6. The peak associated with C–C (284.6 eV) becomes predominant, while the peaks related to the oxidized carbon species such as C–OH (285.2 eV), C–O (286.7 eV), and O–

C=O (288.4 eV) are greatly weakened. This finding indicates that GO was strongly deoxygenated and reduced to graphene. The Ce 3d binding energy peaks, such as those at 881.9 and 900.4 eV, are consistent with the Ce 3d_{3/2} and 3d_{5/2} states, respectively.³² The major peaks at 70.6 and 73.9 eV can be assigned to the 4f_{7/2} and 4f_{5/2} Pt metal states, respectively.³⁴ The IR spectra are shown in Figure S15 of the Supporting Information. The disappearance of the C=O vibration (1729 cm^{−1}) of the COOH groups, as well as the appearance of only one new C=O band (1643 cm^{−1}), indicate that the Pt@CeO₂ nanospheres are covalently bonded to the surface of RGO.

2.2.3. Chemical Reduction of Nitrophenol by Ammonia Borane (AB, NH₃BH₃). In most of traditional hydrogenation reactions, H₂ gas and NaBH₄ are used as the sources of hydrogen. For a H₂-based catalytic reaction, their application is severely limited by two disadvantages. The first disadvantage is the storage problem, and the other is the need for pressurized conditions. Under atmospheric pressure, the catalytic reaction is difficult to achieve using H₂, as the activation of H₂ on noble metal surfaces requires highly pressurized conditions, which are very dangerous. For a NaBH₄-based catalytic reaction, instability makes the reaction unsuitable for practical applications. As a hydrogen reservoir, AB has drawn much attention due to its high hydrogen capacity of 19.6 wt %, strong stability, and nontoxicity.^{35–38} Thus, a new, safe hydrogenation reaction, using AB to replace NaBH₄ or H₂ gas in the catalytic liquid-phase reduction of *p*-nitrophenol (4-NP), has been developed; the catalytic properties of our prepared hybrid catalysts in this hydrogenation reaction are well-tested. It is well-known that the 4-NP solution exhibits a strong absorption peak at 317 nm under neutral or acidic conditions. As the alkalinity of the solution increases, 4-NP ions become the dominant species, producing a spectral shift to 400 nm.³⁹ As shown in Figure 7A, the absorption peak of 4-NP in AB solution is at 317 nm, indicating strong stability of the AB compound in water in the absence of catalysts. After the Pt@CeO₂/RGO hybrids were added, the absorption intensity at 400 nm gradually increased. At the same time, the peak at 317 nm dropped rapidly. The acid ionization constants of water and 4-NP are 15.7 and 7.08 (22 °C), respectively. The acidity of 4-NP is much stronger than that of water. At the beginning of the catalytic reaction, the H⁺ ions dissociated from 4-NP to react with AB and generate H₂, leaving the 4-NP anions. This reaction is consistent with the shift of the absorption peaks from 317 to 400 nm; some bubbles were obvious in the reactor. Approximately 2 min later, the absorption intensity at 400 nm reached a maximum (Figure 7A), and then the absorption peak intensity at 400 nm began to decrease linearly. The similar ionization process could also be observed in 2,3-NP system. As shown in Figure S17 of the Supporting Information (*m*-nitrophenol, 3-NP) and Supporting Information Figure S18, (*o*-nitrophenol, 2-NP), compared with 4-NP molecule, the transform from NP to NP anion become very fast. The whole process is finished within 25 s for 3-NP. The initial catalytic rate was very fast, and the rate gradually slowed. Meanwhile, the bright yellow solution completely faded and became colorless. Figure 7B shows ln(C/C_{0,4-NP}) (C and C_{0,4-NP} represent the concentration of 4-NP at time (*t*) and at the beginning of the reaction, respectively) versus time at different catalyst concentrations; *T* = 24 °C. A rapid and almost linear evolution is observed between *t* and ln(C/C_{0,4-NP}), indicating that this catalytic reaction is a typical first-order reaction for the concentration of 4-NP. Increasing the catalyst concentration

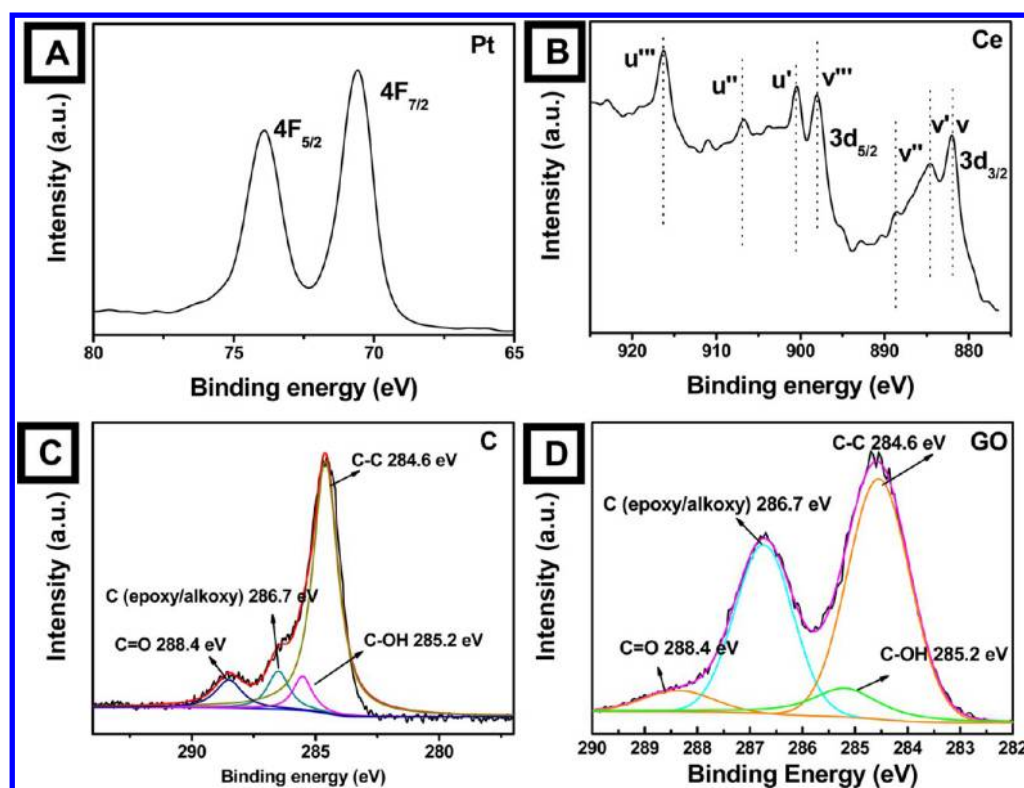


Figure 6. XPS spectra of (A) element Pt; (B) element Ce; (C) element C in Pt@CeO₂/RGO; and that of element C in GO (D).

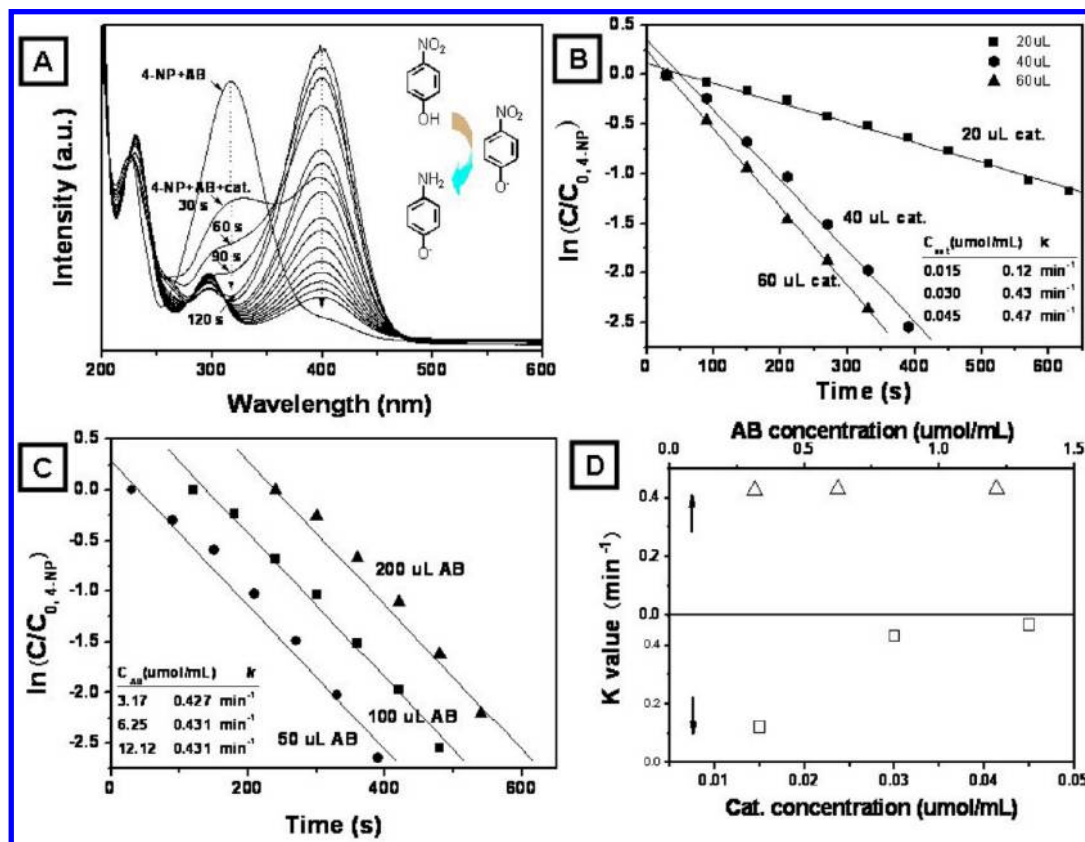


Figure 7. (A) Successive UV-vis absorption spectra showing the reduction of 4-NP by AB. (B) Plot of time vs $\ln(C/C_{0,4-NP})$ by Pt@CeO₂/RGO at different catalyst concentrations (AB: 0.1 mL, T : 24 °C). (C) Plot of time vs $\ln(C/C_{0,4-NP})$ by Pt@CeO₂/RGO at different AB concentrations (catalyst: 0.04 mL, T : 24 °C). (D) Relationship between $\ln k$ and AB or catalyst concentration.

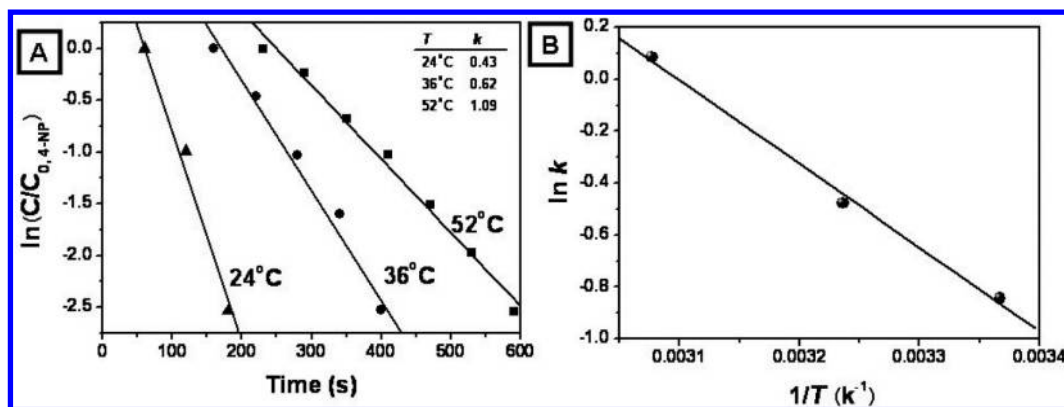


Figure 8. (A) Plot of time vs $\ln(C/C_{0,4-NP})$ by Pt@CeO₂/RGO at different temperatures (AB: 0.1 mL, catalyst: 0.04 mL); (B) Arrhenius plot of $\ln k$ vs $(1/T)$.

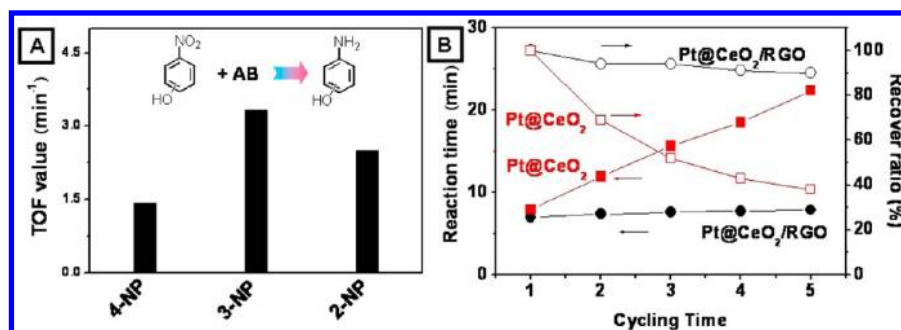


Figure 9. (A) TOF in the catalytic reduction of *o*-, *m*-, and *p*-nitrophenol (2-, 3-, and 4-NP, respectively) by AB compound (AB: 0.1 mL, T: 24 °C, catalyst: 0.04 mL); (B) reaction time and recover ratio in successive reaction cycles for Pt@CeO₂/RGO (black line) and Pt@CeO₂ (red line).

dramatically increases the catalytic rate. The rate constant k can be calculated from the rate equation $\ln(C/C_{0,4-NP}) = kt$. The plot of $\ln(C/C_{0,4-NP})$ versus time at various AB concentrations is also shown in Figure 7C. Interestingly, increasing the concentration of AB did not increase the catalytic rate, because the k value remained almost constant. The nearly horizontal line indicates that the reaction catalyzed by the Pt@CeO₂/RGO hybrids is zero-order with respect to the concentration of AB. The 4-NP molecules were totally converted until the molar ratio of AB/4-NP was greater than 5. The relationship between k and the concentration of AB or the catalyst is illustrated in Figure 7D.

Figure 8 shows the plot of $\ln(C/C_{0,4-NP})$ at various temperatures. The values of k at various temperatures are calculated from the slope of the linear part of each plot in Figure 8A to determine the activation energy. Figure 8B shows the linear fitting of $\ln k$ and $1/T$. The apparent activation energy (E_a) can be calculated from the Arrhenius equation:

$$\ln k = \ln A - E_a/RT$$

The calculated E_a value is approximately 30.31 kJ/mol, where $\ln A$ is the intercept of the line and R is the gas constant).

The approximate turnover frequency (TOF) is shown for comparison in Figure 9A, which is calculated as the number of moles of reduced NP per mole of Pt atoms per minute when the conversion reaches 90%. Among the three substrate molecules, the as-obtained Pt@CeO₂/RGO samples exhibited the best catalytic activity for 3-NP, but the worst catalytic activity for 4-NP.

Although recyclability is usually regarded as an advantage of nanoparticle-based heterogeneous catalysts, the practical

application of these catalysts in liquid-phase reactions is still limited by both low efficiency of separation and degradation of catalytic activity resulting from nanoparticle aggregation. In a previous study, Yin's group overcame this problem by introducing Fe₃O₄ to form hybrids with noble metals and further coating the hybrids with a porous SiO₂ layer.⁴⁰ The synthesis of a layer-by-layer nanostructure was complex and required a high level of skill. Recently, the development of graphene-based technologies has provided a facile way to solve this problem, that is, the self-assembly of various functional components on graphene. The importance of graphene can be attributed to two factors. The first is the hard template-effect, in which monolayer sheets with large surface areas fix and separate the active components from each other, which is very helpful for maintaining their shape and size during the catalytic reaction. The other is the restriction of the Brownian motions of the small particles after they form hybrids with RGO, which allows the catalysts to be recycled after the catalytic. The cycling test was thus performed to study the recyclability of Pt@CeO₂ and Pt@CeO₂/RGO. Since the TOF value is inversely proportional to the reaction time and the mass of the catalyst

$$\text{TOF} \propto 1/(t \cdot m)$$

(where t is the reaction time when 90% of 4-NP were reduced and m is the mass of the catalyst); thus if it were constant, the decrease of m should result in the increase of reaction time. In Figure 9B, the time-evolution curves clearly demonstrate this relationship, and the two catalysts exhibit very similar catalytic activities in the first cycle. Notice that Pt@CeO₂ was recovered from the solution by centrifugation before every new cycle;

however, a great mass of Pt@CeO₂ can not be separated due to its rather good water solubility, and there remains only 38% of Pt@CeO₂ in weight after five cycles. While in the case of Pt@CeO₂/RGO, its poor colloidal stability in water make the collection much easier, and its recover ratio reaches to about 90%. After careful calculation for each cycle, it is found that the TOF values remained almost constant as 1.44 min⁻¹ for Pt@CeO₂/RGO and 1.22 min⁻¹ for Pt@CeO₂. The result firmly indicates that the as-obtained core@shell superstructure is rather stable. The weight loss rather than degradation of catalysts is the true reason why the catalytic reaction time was prolonged as the cycling numbers increased. Moreover the support of RGO greatly improves the recyclability of Pt@CeO₂ for liquid-phase catalysis.

3. CONCLUSIONS

In all, we have successfully prepared pomegranate-like Pt@CeO₂ multicore@shell nanospheres in a large scale via a facile nonorganic route. Without addition of any reducing agents or surfactants, the whole reaction is a clean redox process that happens between Ce(NO₃)₃ and K₂PtCl₄ in an alkaline aqueous solution. These uniform Pt@CeO₂ hybrid nanospheres are completely built up by spontaneous self-assembly of naked Pt and CeO₂ nanoparticles (the detailed comparisons with previous methods are shown in Table S2 of the Supporting Information). Control experiments confirm that such a hybrid structure formation is related to the balanced growth of the Pt and CeO₂. Once the proper balance is broken, no regular nanospheres can be formed. In the catalytic test of oxidation of CO into CO₂, the as-obtained Pt@CeO₂ hybrid nanospheres exhibited rather high activity and thermal stability. Even after calcination at 600 °C for 5 h in air, they efficiently catalyzed 100% conversion of CO into CO₂ at a relatively low temperature (145 °C). The Pt@CeO₂ multicore@shell nanospheres can be further supported on RGO nanosheets to form Pt@CeO₂/RGO nanocomposites. Kinetic studies on Pt@CeO₂/RGO revealed that the catalytic reduction of 4-NP was first-order with respect to substrate concentration and zero-order with respect to AB concentration. The activation energy for the hydrolysis reaction was 30.31 kJ/mol. In addition, the Pt@CeO₂/RGO sample showed a desirable degree of recyclability. Such a fast, green, and large-scale synthetic strategy has great significance for the design and preparation of highly active and stable catalysts in real-world applications.

4. EXPERIMENTAL SECTION

4.1. Synthesis of GO. GO was synthesized from natural graphite powder according to a modified Hummers method.⁴¹ Briefly, 0.9 g of graphite powder was added into a mixture of 7.2 mL of 98% H₂SO₄, 1.5 g of K₂S₂O₈, and 1.5 g of P₂O₅. The solution was kept at 80 °C for 4.5 h, followed by thorough washing with water. Thereafter, the as-treated graphite was put into a 250 mL beaker, to which 0.5 g of NaNO₃ and 23 mL of H₂SO₄ (98%) were then added while keeping the beaker in the ice bath. Subsequently, 3 g of KMnO₄ was added slowly. After 5 min, the ice bath was removed and the solution was heated up to and kept at 35 °C under vigorous stirring for 2 h, followed by the slow addition of 46 mL of water. Finally, 40 mL of water and 5 mL of H₂O₂ was added, followed by water washing and filtration. The exfoliation of graphene oxide was then dispersed in water (5 mg mL⁻¹) under ultrasonication for 2 h to yield a homogeneous suspension.

4.2. Synthesis of Pt@CeO₂ Multicore@Shell Nanospheres. The whole synthetic process was performed under Ar protection. A 1 mL aliquot of 0.1 M Ce(NO₃)₃ was added to 10 mL of H₂O, and then

Ar was bubbled into the solution for 10 min. Then, 1 mL of a 0.2 M NaOH aqueous solution was rapidly added, followed immediately by the quick addition of 1 mL of 0.01 M K₂PtCl₄. The solution was heated at 70 °C for 1 h. After being cooled to room temperature, the sample was purified by centrifugation to remove the residual unassembled bare CeO₂ nanoparticles, which remained in the supernatant solution. Finally, the as-obtained samples were directly dried at 80 °C overnight.

The large-scale synthesis was similar to the above procedure, just with larger volumes of the solutions being used. Under Ar protection, 10 mmol Ce(NO₃)₃ was dissolved in 500 mL of water, followed by the addition of 10 mL of 2 M NaOH solution and 10 mL of 0.1 M K₂PtCl₄. The other conditions were the same as in the above procedure.

4.3. Synthesis of Pure CeO₂ Nanoparticles. The synthesis was the same as the above process, except there was no K₂PtCl₄ added.

4.4. Synthesis of PVP-Stabilized Pt Nanoparticles. A 10 mL volume of 10 mM H₂PtCl₆ was mixed with 10 mL of a 50 mM PVP/EG solution, followed by hydrothermal treatment at 140 °C for 4 h. The sample was purified by centrifugation with the help of acetone.

4.5. Synthesis of Pt-CeO₂-GO Ternary Hybrid Nanocomposites. The whole synthetic process was performed under Ar protection. A 1 mL aliquot of 0.1 M Ce(NO₃)₃ was added to 10 mL of H₂O, followed by the addition of 2 mL of the GO solution, and the mixture was then bubbled with Ar for 10 min. Next, 1 mL of 0.2 M NaOH aqueous solution was rapidly added, followed immediately by the addition of 1 mL of 0.01 M K₂PtCl₄. The solution was heated at 70 °C for 1 h. After being cooled to room temperature, the sample was purified by centrifugation and directly dried at 80 °C overnight without any washing.

4.6. Synthesis of Sample 4. The PVP-stabilized Pt and pure CeO₂ nanoparticles were mixed together in the same molar ratio as that of Pt and Ce in Sample 1. After ultrasonic treatment for 10 min, the sample was purified by centrifugation with the help of acetone.

4.7. Synthesis of Pt@CeO₂/RGO. The process is similar to that for preparation of Pt@CeO₂ nanospheres except for the introduction of GO. In details the whole synthetic process was taken under Ar protection. Twenty milliliters of H₂O was heated at 70 °C for 10 min, then 2 mL of Ce(NO₃)₃ solution (0.1 mmol/mL) was added followed by addition of 0.4 mL NaOH (1 mmol/mL). Two milliliters of K₂PtCl₄ was injected immediately. The color of the solution became black within 30 s. Five minutes later, 1 mL of GO solution was further injected in. The solution was kept at 70 °C for 60 min.

4.8. Heat Treatment. The calcination was performed in air at a heat rate of 5 °C/min.

4.9. Characterization. The X-ray diffraction patterns of the products were collected on a Rigaku-D/max 2500 V X-ray diffractometer with Cu-K_α radiation (λ = 1.5418 Å), with an operation voltage and current maintained at 40 kV and 40 mA. Transmission electron microscopic (TEM) images were obtained with a TECNAI G2 high-resolution transmission electron microscope operating at 200 kV. XPS measurement was performed on an ESCALAB-MKII 250 photoelectron spectrometer (VG Co.) with Al K_α X-ray radiation as the X-ray source for excitation.

4.10. Catalytic Test. **4.10.1. CO Oxidation.** Eight milligrams of catalysts were mixed with 20 mg of SiO₂. The mixture was put in a stainless steel reaction tube. The experiment was carried out under a flow of reactant gas mixture (1% CO, 20% O₂, balance N₂) at a rate of 30 mL/min. The composition of the gas was monitored online by gas chromatography (GC 9800).

4.10.2. Chemical Reduction of NP by AB. The catalytic test was directly taken in a quartz cuvette in the UV/vis/NIR spectrophotometer. The aqueous solutions of *o*-, *m*-, and *p*-nitrophenol (0.01 mmol/mL, abbreviated as 2-, 3-, and 4-NP, respectively) and AB (0.2 mmol/mL) were freshly prepared. Typically 0.1 mL of nitrophenol and 0.1 mL of AB aq were mixed in 3 mL of H₂O. Then 40 μL of catalysts (0.0025 mmol/mL, calculated from Pt, determined by ICP) were quickly added. The intensity of the absorption peak at 400 nm for 4-NP (410 nm for 2-NP and 330 nm for 3-NP) was monitored by UV-vis spectroscopy along with time. All the samples were

thoroughly washed and purified by centrifugation before a next catalytic cycle.

■ ASSOCIATED CONTENT

■ Supporting Information

XRD, EDX, XPS and size distribution histogram of the Pt@CeO₂ nanospheres; TEM images of PVP stabilized Pt nanoparticles; control experiment by using Ce(IV) instead of Ce(III); TEM images and photos of Samples 4 and 5; TEM image of the Pt@CeO₂ nanospheres after five cycling tests; photos of Pt@CeO₂ and Pt@CeO₂/RGO in water; schematic synthesis process of the Pt@CeO₂/RGO; XRD, IR, EDX, and UV–vis absorption spectrum of Pt@CeO₂/RGO; TEM image of Pt@CeO₂/RGO after five cycles; UV–vis absorption spectra during the process of the reduction of 3-NP/2-NP by AB; the summary of Pt-CeO₂ hybrid systems prepared from different methods. This material is available free of charge via the Internet at <http://pubs.acs.org>.

■ AUTHOR INFORMATION

Corresponding Author

hongjie@ciac.ac.cn

Notes

The authors declare no competing financial interest.

■ ACKNOWLEDGMENTS

The authors are grateful for the financial aid from the National Natural Science Foundation of China (Grant Nos. 21001101, 21071140, 51272249, 91122030, and 21210001), '863'-National High Technology Research and Development Program of China (Grant No. 2011AA03A407), and National Natural Science Foundation for Creative Research Group (Grant No. 21221061).

■ REFERENCES

- (1) Yu, T.; Zeng, J.; Lim, B.; Xia, Y. N. *Adv. Mater.* **2010**, *22*, 5188.
- (2) Zhou, H. P.; Wu, H. S.; Shen, J. A. X.; Yin, L. D.; Sun, C. H.; Yan, J. *Am. Chem. Soc.* **2010**, *132*, 4998.
- (3) Yoon, K.; Yang, K.; Lu, P.; Wan, D.; Peng, H.; Masias, K.; Fanson, P.; Campbell, C.; Xia, Y. N. *Angew. Chem., Int. Ed.* **2012**, *51*, 9543.
- (4) Chu, Y. Y.; Wang, Z. B.; Jiang, Z. Z.; Gu, D. M.; Yin, G. P. *Adv. Mater.* **2011**, *23*, 3100.
- (5) Schweitzer, N. M.; Schaidle, J. A.; Ezekoye, O. K.; Pan, X. Q.; Linic, S.; Thompson, L. T. *J. Am. Chem. Soc.* **2011**, *133*, 2378.
- (6) Anumol, E. A.; Kundu, P.; Deshpande, P. A.; Madras, G.; Ravishankar, N. *ACS Nano* **2011**, *5*, 8049.
- (7) Perkas, N.; Rotter, H.; Vradman, L.; Landau, M. V.; Gedanken, A. *Langmuir* **2006**, *22*, 7072.
- (8) Yu, X.; Kuai, L.; Geng, B. Y. *Nanoscale* **2012**, *4*, 5738.
- (9) Trogadas, P.; Parrondo, J.; Ramani, V. *Chem. Commun.* **2011**, 11547.
- (10) Arnal, P. M.; Comotti, M.; Schuth, F. *Angew. Chem., Int. Ed.* **2006**, *45*, 8224.
- (11) Wen, C.; Zhu, Y.; Ye, Y.; Zhang, S.; Cheng, F.; Liu, Y.; Wang, P.; Tao, F. *ACS Nano* **2012**, *6*, 9305.
- (12) Chen, C.; Nan, C.; Wang, D.; Su, Q.; Duan, H.; Liu, X.; Zhang, L.; Chu, D.; Song, W.; Peng, Q.; Li, Y. D. *Angew. Chem., Int. Ed.* **2011**, *50*, 3725.
- (13) Qi, J.; Chen, J.; Li, G. D.; Li, S. X.; Gao, Y.; Tang, Z. Y. *Energy Environ. Sci.* **2012**, *5*, 8937.
- (14) Sun, C. W.; Li, H.; Chen, L. Q. *Energy Environ. Sci.* **2012**, *5*, 8475.
- (15) Seh, Z. W.; Liu, S. H.; Zhang, S. Y.; Shah, K.; Han, M. Y. *Chem. Commun.* **2011**, 47, 6689.

- (16) Seh, Z. W.; Liu, S. H.; Low, M.; Zhang, S. Y.; Liu, Z. L.; Mlayah, A.; Han, M. Y. *Adv. Mater.* **2012**, *24*, 2310.
- (17) He, L. C.; Liu, Y.; Liu, J. Z.; Xiong, Y. S.; Zheng, J. Z.; Liu, Y. L.; Tang, Z. Y. *Angew. Chem., Int. Ed.* **2013**, *52*, 3741.
- (18) Wang, L. X.; Yang, J. D.; Yin, H. J.; Song, R.; Tang, Z. Y. *Adv. Mater.* **2012**, *25*, 2728.
- (19) Lee, I.; Joo, J. B.; Yin, Y. D.; Zaera, F. *Angew. Chem., Int. Ed.* **2011**, *50*, 10208.
- (20) Chen, C.; Fang, X. L.; Wu, B. H.; Huang, L. J.; Zheng, N. F. *ChemCatChem* **2012**, *4*, 1578.
- (21) Zhang, N.; Fu, X. Z.; Xu, Y. J. *J. Mater. Chem.* **2011**, *21*, 8152.
- (22) Du, J.; Qi, J.; Wang, D.; Tang, Z. Y. *Energy Environ. Sci.* **2012**, *5*, 6914.
- (23) Xi, G. C.; Ye, J. H.; Ma, Q.; Su, N.; Bai, H.; Wang, C. J. *Am. Chem. Soc.* **2012**, *134*, 6508.
- (24) Yin, H.; Tang, H. J.; Wang, D.; Gao, Y.; Tang, Z. Y. *ACS Nano* **2012**, *6*, 8288.
- (25) Kim, K. W.; Kim, S. M.; Choi, S.; Kim, J.; Lee, I. S. *ACS Nano* **2012**, *6*, 5122.
- (26) Kayama, T.; Yamazaki, K.; Shinjoh, H. *J. Am. Chem. Soc.* **2010**, *132*, 13154.
- (27) Mitsudome, T.; Mikami, Y.; Matoba, M.; Mizugaki, T.; Jitsukawa, K.; Kaneda, K. *Angew. Chem., Int. Ed.* **2012**, *51*, 136.
- (28) Wang, X.; Li, X. Y.; Liu, D. P.; Song, S. Y.; Zhang, H. J. *Chem. Commun.* **2012**, 48, 2885.
- (29) Wang, X.; Liu, D. P.; Song, S. Y.; Zhang, H. J. *Chem. Commun.* **2012**, 48, 10207.
- (30) Wang, X.; Liu, D. P.; Song, S. Y.; Zeng, L.; Zhang, Y. *Dalton Trans.* **2012**, 41, 7193.
- (31) Li, X. Y.; Huang, X. L.; Liu, D. P.; Wang, X.; Song, S. S.; Zhou, L.; Zhang, H. J. *J. Phys. Chem. C* **2011**, *115*, 21567.
- (32) Li, X. Y.; Wang, X.; Song, S.; Zhang, H. J. *Chem.—Eur. J.* **2012**, *18*, 7601.
- (33) Wang, X.; Liu, D. P.; Song, S. Y.; Zhang, H. J. *Chem.—Eur. J.* **2013**, *19*, 8082.
- (34) Wagner, C. D.; Riggs, W. M.; Davis, L. E.; Moulder, J. F.; Muilemberg, G. E. *Handbook of X-Ray Photoelectron Spectroscopy*; Perkin-Elmer Corporation, 1979.
- (35) Hamilton, C. W.; Baker, R. T.; Staubitz, A.; Manners, I. *Chem. Soc. Rev.* **2009**, 38, 279.
- (36) Mohajeri, N.; Raissi, A.; Adebisi, O. *J. Power Sources* **2007**, *167*, 482.
- (37) Chandra, M.; Xu, Q. *J. Power Sources* **2006**, *159*, 855.
- (38) Marder, T. B. *Angew. Chem., Int. Ed.* **2007**, *46*, 8116.
- (39) Zeng, J.; Zhang, Q.; Chen, J. Y.; Xia, Y. N. *Nano Lett.* **2010**, *10*, 30.
- (40) Ge, J. P.; Zhang, Q.; Zhang, T. R.; Yin, Y. D. *Angew. Chem., Int. Ed.* **2008**, *47*, 8924.
- (41) Seng, K. H.; Guo, Z. P.; Chen, Z. X.; Liu, H. K. *Adv. Sci. Lett.* **2011**, *4*, 18.